



This is the accepted manuscript made available via CHORUS. The article has been published as:

Surface anisotropic magnetoresistance in the antiferromagnetic semiconductor math xmlns="http://www.w3.org/1998/Math/MathML">mrow>mi > Cr/mi>msub>mi>Sb/mi>mn>2/mn>/msub>/mrow>/math>

K. Nakagawa, M. Kimata, T. Yokouchi, and Y. Shiomi Phys. Rev. B **107**, L180405 — Published 30 May 2023

DOI: 10.1103/PhysRevB.107.L180405

Surface anisotropic magnetoresistance in antiferromagnetic semiconductor CrSb₂

K. Nakagawa¹, M. Kimata², T. Yokouchi¹ and Y. Shiomi¹

¹Department of Basic Science, The University of Tokyo, Tokyo 153-8902, Japan

²Institute for Materials Research, Tohoku University, Sendai, Miyagi, 980-8577, Japan

Abstract

We report large anisotropic magnetoresistance in surface states of an antiferromagnetic semiconductor CrSb₂. The low-temperature measurement of angle-dependent magnetoresistance (ADMR) is performed in high magnetic fields up to 24 T. At 1.4 K where the surface conduction is dominant, ADMR exhibits clear two-fold symmetry consistent with anisotropic magnetoresistance (AMR) due to magnetic-field induced change of antiparallel magnetic structure. The AMR magnitude reaches 9.3% despite the small angle dependence of the net magnetic moments, suggesting strong spin orbit interaction in the surface conduction layer.

Introduction- Narrow-gap semiconductors have long been studied in condensed matter physics because of their unique properties, such as large thermoelectric effects [1], various optical effects [2–4], and giant magneto-transport effects [5–7]. Recently, surface states possibly showing up in narrow-gap semiconductors have newly attracted attention not only from the viewpoint of fundamental physics but also from next-generation electronics applications. Notable examples of these material class are topological insulators [8,9] and topological Kondo insulators [10–12], where the gapped bulk states host metallic surface states because of topological origins. The topological surface state is non-magnetic, but the electric current flowing on the surface is highly spin polarized. Spin-polarized transport on the surface is promising for applications in spintronics devices [13,14].

CrSb₂ which we focus on here is a narrow-gap semiconductor with a marcasite crystal structure, similar to FeSb₂, a topological Kondo insulator candidate [13-18]. Contrary to the fact that the resistivity of conventional semiconductors diverges as temperature approaches zero, CrSb₂ and FeSb₂ both show a resistivity plateau below ~10 K, which can be attributed to metallic conduction of surface states [Fig. 1(a)] [19,20]. Despite the similar zero-field transport properties, CrSb₂ shows a collinear antiferromagnetic (AF) order with quasi-one-dimensional magnons [18,21,22], while FeSb₂ is non-magnetic. Recently, Q. Du *et al.* investigated the CrSb₂ surface states in detail and suggested from the band structure calculation that the surface state of CrSb₂ is not of topological origins, and possibly magnetic [19]. Such magnetic surface states are not expected in conventional topological surface states, and hence the CrSb₂ surface state is unique in condensed matter physics

as well as spintronics. Its magnetoresistive response is particularly interesting not only for the study of magnetic surface properties but also for electrical readout technique of magnetic states, but the magnetism and magnetotransport properties of the CrSb₂ surface state have been hardly studied so far.

In this work, we experimentally show that CrSb₂ has an antiferromagnetic surface state with strong spin-orbit interaction by angle-dependent magnetoresistance (ADMR) measurement at low temperatures and in high magnetic fields up to 24 T. The ADMR results show that the sizable anisotropic magnetoresistance (AMR) is apparent at low temperatures where the surface conduction is dominant, whereas at high temperatures above ~10 K, this magneto-transport is masked by ordinary magnetoresistance resulting from the cyclic motion of high-mobility bulk carriers. AMR describes a change of resistance when the magnetization orientation changes with respect to current direction [25]. AMR arises from anisotropic spin-dependent scattering due to spin-orbit interaction [23,24], and antiferromagnetic materials with large AMR have recently been developed in the field of antiferromagnetic spintronics. Some antiferromagnets have been found to show large AMR due to nontrivial mechanisms: *e.g.* field-induced transitions such as spin-flop transition [25] and metal-insulator transition [26], and topologically non-trivial electronic structure [27,28]. However, except these unusual materials of class, conventional collinear antiferromagnets usually exhibit a much smaller AMR than the ferromagnetic AMR [24,29]. Even for MnTe [30] and Fe₂As [31], whose weak in-plane anisotropy allows the Néel vector to be easily rotated by the applied magnetic field, antiferromagnetic AMR signals are at most 2%.

In the surface state of CrSb₂, we observe the clear AMR signal, the magnitude of which increases with magnetic fields and reaches 9.3% at 24 T, notably larger than those expected in conventional collinear antiferromagnets and comparable to those of ferromagnets. Because of the strong uniaxial magnetic anisotropy and exchange coupling constants, the Néel vector of CrSb₂ hardly rotates under the rotating magnetic field, but the antiferromagnetic moments tilt along the magnetic field, potentially giving rise to AMR. The produced net magnetization M is, however, estimated to be only 1.8% of full moment at 24 T. Since the spin-orbit interaction plays a central role in AMR [23,31], we conclude that CrSb₂ has an exotic surface state with antiferromagnetic order and also with strong spin-orbit interaction, which should be unique in the emerging field of antiferromagnetic spintronics.

Methods- Single crystals of CrSb₂ were grown out of an Sb flux as previously described [23]. High-purity Sb and Cr powders with a molar ratio of 94: 6 were charged into a vacuum-sealed quartz ampoule. The mixture was heated to 1000° C over 6 h, kept for 36 h, and then slowly cooled (2° C / h) to 670° C. The quartz ampoule was quickly removed from the furnace and excess Sb was removed by centrifuging. It was confirmed that the transport property of as-grown samples was almost the same for the samples washed with dilute HCl. Hence, the influence of possible Sb flux residues on the surface is negligible. The crystal structure was confirmed by analyzing powder X-ray diffraction patterns taken with Cu K α radiation. The sample used in this study was

oriented with a Laue camera. The largest plane is a-c plane with the dimension of 1.2 mm \times 0.3 mm and the thickness along the b-axis is 0.18 mm. Note that the metallic surface state was confirmed on the a-c crystallographic plane in the previous angle-resolved photoemission spectroscopy (ARPES) measurement [19]. Also, we further confirmed by X-ray fluorescence measurement (Hitachi, EA6000VX) that a sample with the a-c surface is of CrSb₂ stoichiometry. Hereafter, we define the crystallographic c, a, and b-axes as x, y, and z-axes, respectively. For all the transport measurements, the electric current is applied along the c-axis (x-axis). The electrodes were prepared using Au wires and Ag pastes.

ADMR was measured using a two-axis rotator system developed at the High Field Laboratory for Superconducting Materials, Institute for Materials Research, Tohoku University. A cryogen-free superconducting magnet is used to apply magnetic field up to 24 T. The lock-in detection was used for the ADMR measurement with AC electric current of $10~\mu A$. Other transport measurements for sample characterization were conducted using Quantum Design PPMS-9. The standard four-probe technique was used to measure the longitudinal and transverse resistivities. The zero point of the angle in the ADMR measurement was determined using a Hall sensor mounted on a holder for angle calibration.

Results- Figure 1(b) shows the temperature dependence of longitudinal resistivity $\rho_{xxt}(T)$ measured without magnetic field. Weak anomaly is observed at the Néel temperature $T_N \approx 273$ K. As temperature decreases from about 150 K, the resistivity increases by several orders of magnitude, which is ascribed to the bulk semiconducting channel. The hump observed at 50 - 80 K has been attributed to an increase in carrier mobility with decreasing temperature when phonon scattering dominates the carrier relaxation time [19,21]. On further lowering the temperature, $\rho(T)$ becomes weakly temperature-dependent at approximately 13 K and shows a resistivity plateau at lower temperatures. This saturation observed at very low temperatures was recently shown to originate from a metallic surface state by systematic resistivity measurement for samples with different thicknesses combined with ARPES measurement [19]. The temperature dependence of resistivity is well explained by a parallel circuit model consisting of a thermally activated bulk contribution and a temperature-independent surface one [18]: $1/\rho = 1/\rho_0 \exp(-\frac{\Delta}{k_B T}) + 1/\rho_s$, where $\rho_0 \exp(\frac{\Delta}{k_B T})$ is the semiconducting bulk resistivity with a bulk energy gap Δ and ρ_s is the metallic surface state one. The magnitude and overall temperature dependences of resistivity in Fig. 1(b) is consistent with previous reports [13,19,21]. We also confirmed that the temperature dependence of magnetic susceptibility (Fig. S1 in Supplemental Material (SM) [32]) is consistent with a previous report [21].

Figure 1(c) presents the magnetoresistance: MR (%) $\equiv 100 \times \{\rho_{xx}(H) - \rho_{xx}(0 \text{ T})\} / \rho_{xx}(0 \text{ T})$, under magnetic field up to 9 T applied perpendicular to the sample plane $(H \parallel z)$. Above 12 K, conventional positive magnetoresistance due to the Lorentz force is observed because of high mobility of bulk carriers. Large positive magnetoresistance is observed at 20 K, but notably suppressed with decreasing temperature and its sign changes

to negative below 10 K where the surface conduction is dominant. Now that the existence of the surface state has been confirmed, magnetic surface transport is a possible origin of negative magnetoresistance. The mobility of the surface state seems low, as the ordinary magnetoresistance is overwhelmed by magnetic transport.

The temperature dependence of MR at 9 T in Fig.1(d) shows a crossover from bulk-dominant transport to surface-dominant one, consistent with the temperature dependence of resistivity [Fig.1(b)]. Below 10 K, the MR data with applied magnetic fields in three different orthogonal directions are all negative. In contrast, above the crossover temperature, MR changes to positive in all the magnetic-field configurations. For $H \parallel z$ where the effect of the Lorentz force should be most significant, positive MR is highly enhanced and maximized at 30 K with the magnitude of 58%. The large magnetoresistance indicates high carrier mobility in bulk states. As the temperature further increases, the positive MR decreases due to decrease in carrier mobility by phonon scattering, which is consistent with the resistivity hump observed at 50 - 80 K [Fig.1(b)].

The ADMR measurement was performed at low temperatures for three rotational directions as illustrated in Fig. 2(a): α , β , and γ scans. Figure 2(b) shows the ADMR data of α , β , and γ scans measured at 24 T and 1.4 K. At this temperature, conductivity of the bulk state is several orders smaller than that of the surface state, and thus the observed ADMR is safely ascribed to the signals from the surface state.

ADMR exhibits clear two-fold symmetry for α , β , and γ scans. To clarify the relation of the ADMR results to the surface magnetic properties, we calculated the magnetization directions under rotating magnetic fields and estimated the AMR signals in Fig. 2(c). Since the magnetic property on the surface state is unknown, we assume that the surface spin-Hamiltonian is the same as bulk one [22]:

$$\mathcal{H} = \sum_{\alpha} \sum_{\langle ij \rangle_{\alpha}} J_{\alpha} \mathbf{S}_i \cdot \mathbf{S}_j + \sum_{i} D(S_{\mathrm{EA}}^2)_i + \gamma_e \hbar \sum_{i} \mathbf{S}_i \cdot \mathbf{H},$$

where J_a , S_i , D, S_{EA} , and H are exchange interaction constant, spin operator, uniaxial anisotropy parameter, projection of spin operator to the easy-axis, and applied magnetic field, respectively. α is summed over the crystallographic a, b, and c axes. The index i (j) indicates the antiferromagnetic sublattice, and $\langle ij \rangle_{\alpha}$ is summed over nearest neighbor atom positions for each crystallographic axis. Magnetic easy-axis is perpendicular to the (101) plane, i.e., tilted by 61.5° from the c-axis to the a-axis [18,22]. The parameters determined by neutron experiments are $J_c = 35.7$ (2), $J_a = -1.31$ (6), $J_b = 1.69$ (7), and D = 2.07 (9) meV [22]. Based on this Hamiltonian, we calculated the spin direction of each sublattice that minimizes the total energy. The main terms are the exchange interaction and anisotropy, and the Zeeman term is small due to small net moments. In the calculation, two possible magnetic domains with different easy-axis configurations are assumed to be equal and averaged.

The AMR signal is estimated to be proportional to the square of the field-induced net magnetization along the current direction: $\rho^{AMR}_{xx} \propto M_x^2$. The simulated M_x^2 , shown in Fig. 2(c), exhibits sinusoidal angle dependence with two-fold symmetry. The overall angle dependence is qualitatively consistent with the ADMR results shown in Fig. 2(b). In contrast to ferromagnetic materials in which magnetization is fully aligned along the magnetic

field direction, the antiferromagnetic configuration is hardly changed by magnetic field due to the exchange interaction along the *c*-axis (~36 meV) that is much greater than the Zeeman energy. The magnetic-field strength necessary for the spin-flop transition is calculated to be 38.3 T, much larger than the current maximal magnetic field. Also, the Néel vector of CrSb₂ hardly rotates in tune with magnetic field because of strong uniaxial anisotropy (~2 meV). The spin configuration of CrSb₂ remains almost unchanged regardless of the direction of the magnetic field, and the resulting net magnetization is as small as 1.8% of full moment even at 24 T. Hence, the slight change in the magnetic moment vectors result in the large AMR. This is also the case when the AMR is caused by magnetic-field change in the Néel vector. We confirmed by the calculation that the observed AMR can be explained by the Néel vector if the AMR coefficient is negative (see Fig. S2 in SM [32]). Although the origin of the surface state in CrSb₂ is not topological, the symmetry breaking at the surface and the heavy constituent element Sb may enhance the spin-orbit interaction effect and result in the large surface AMR.

To understand the AMR results in relation to the magnetic structure, field-induced canted magnetic moments in the xy plane are illustrated in Fig. 2(d). In zero magnetic field, collinear antiferromagnetic moments are aligned along the easy-axis, which is tilted 61.5° from the x-axis; there should be two magnetic domains with the easy-axes of $+61.5^{\circ}$ and -61.5° . Since the exchange interaction and uniaxial anisotropy are strong, the antiferromagnetic moments are only canted slightly by applying a magnetic field. When the magnetic field rotates within the xy plane (α scan), M_x is maximized at $H \parallel x$ ($\alpha = 0^{\circ}$) and minimized at $H \parallel y$ ($\alpha = 90^{\circ}$), resulting in the larger AMR signal at $\alpha = 0^{\circ}$. Note that if the proportions of the two domains differ by 10%, the α dependence does not change its shape but only shifts its phase by a few degrees; this small phase shift is indistinguishable from sample misalignment in the present experiment. In applying the magnetic field along the perpendicular direction ($H \parallel z$), the antiferromagnetic moments tilt along the z-axis, and M_x is zero. Therefore, the AMR signal is the smallest for $\beta = 0^{\circ}$ and $\gamma = 0^{\circ}$ in β and γ scans. Here we point out that, although the magnetic parameters of the surface state have not been investigated, the calculation will reproduce the experimental results regardless of the parameter values in case that exchange interaction and uniaxial anisotropy are greater than the energy scale of magnetic field.

The magnetic-field dependence of the ADMR data at 1.4 K is shown in Fig. 3(a), where the ADMR data of α scan is plotted at different magnetic fields. The angle dependence is similar throughout the magnetic field regime, and the ADMR magnitude $\{\rho_{xx}(\alpha=0^\circ) - \rho_{xx}(\alpha=90^\circ)\} / \rho_{xx}(\alpha=0^\circ)$ increases monotonically with magnetic fields. The magnetic field dependence of the ADMR magnitude is well fitted with a quadratic function as shown in Fig. 3(b). This quadratic dependence is consistent with the magnetic field dependence of AMR. Net magnetization arises in proportion to the magnetic field strength, resulting in $\rho^{AMR}_{xx} \propto M_x^2 \propto H^2$. We confirmed by the magnetization measurement and also by the calculation that the magnetization appears in proportion to H up to 24 T (see Figs. S1 and S4 in SM [32]).

Temperature dependence of ADMR of γ scan shows crossover from the surface to bulk conduction, as shown in Figs. 3(c) and 3(d). At $\gamma = 0^{\circ}$ (*i.e.* magnetic field perpendicular to the sample plane), the effect of the Lorentz force should be the most significant. At 1.4 K, however, the ADMR magnitude $\{\rho_{xx}(\gamma = 90^{\circ}) - \rho_{xx}(\gamma = 0^{\circ})\}$ / $\rho_{xx}(\gamma = 0^{\circ})$ takes maximum at $\pm 90^{\circ}$ because of large contribution of the AMR. As the temperature increases, this AMR signal decreases, and the sign changes from positive to negative at T = 15 K. At high temperatures, the ADMR magnitude shows maximum at $\gamma = 0^{\circ}$. Here, the ordinary magnetoresistance due to the Lorenz force overwhelms the surface AMR and the ADMR is well explained by the high-mobility bulk transport. This result is also consistent with the MR data shown in Figs. 1(c) and 1(d). As shown in Fig. 3(d), the magnitude of the positive MR reaches approximately 50% at T = 30 K. This magnitude is similar to the results taken at PPMS in Fig. 1(d).

Finally, to further confirm the surface AMR at low temperatures, we additionally performed the ADMR measurement for the transverse resistivity (i.e., the measurement of planar Hall effect) at the lowest temperature. Figure 4 shows the transverse ADMR obtained at 1.9 K when the magnetic field of 21 T is rotated within the xy plane (α scan). Here, after subtracting the influence of misalignment by $\rho^{\text{ave}}_{yx}(\alpha) = \{\rho^{\text{raw}}_{yx}(\alpha) + \rho^{\text{raw}}_{yx}(\alpha)\}$ $\rho^{\text{raw}}_{yx}(\alpha + 180^{\circ})$ \}/2, we further anti-symmetrize ρ^{ave}_{yx} with respect to 0° : $\rho_{yx}(\alpha) = \{\rho^{\text{ave}}_{yx}(+\alpha) - \rho^{\text{ave}}_{yx}(-\alpha)\}$ /2, to eliminate the magnetoresistance due to the misalignment of electrodes (see Fig. S5 in SM [32] for raw data). Because the sample is small and not precisely rectangular, misalignment was inevitable in the electrode positions. The angle dependence of ρ_{yx} shows clear two-fold symmetry with the maximum roughly at 45° (and -135°). In our simulation, the transverse AMR effect is estimated to be $\rho^{AMR}_{\nu x} \propto M_x M_{\nu}$, yielding the angle dependence of $\rho^{AMR}_{\nu x} \sim \sin 2 \alpha$. The experimental data are well fitted with this simulation result as shown in Fig. 4. Note that a transverse AMR of opposite sign is expected from the Néel vector for the AMR coefficient with the positive sign (Fig. S2 in SM [32]), similar to the case of the longitudinal AMR. It is interesting to point out that the transverse ADMR (Fig. 4) is almost half the magnitude of the longitudinal ADMR [Fig. 2(b)]. The different magnitudes of longitudinal and transverse ADMR suggest possible contribution from spin-Hall magnetoresistance [33] which can show up at low temperatures by the interaction of surface carriers with the bulk antiferromagnetic moments (see Fig. S3 in SM [32]; see also references [34,35] therein).

Conclusion- In summary, we performed low-temperature measurement of ADMR under high magnetic fields up to 24 T to explore magneto-transport responses in the surface state of CrSb₂. At 1.4 K, where the surface conduction is well dominant, ADMR at 24 T exhibits a clear two-fold symmetry consistent with the AMR due to the slight change in the magnetic moment vectors by the magnetic field. Because of the strong uniaxial magnetic anisotropy, the net moments induced by the applied magnetic field are estimated to be at most 1.8% of full moment by the numerical simulation incorporating the magnetic parameters of CrSb₂. The measurement of temperature and magnetic-field dependence of ADMR and the additional measurement of the planar Hall effect at 21 T also corroborate the magnetic surface transport of CrSb₂. The sizable magnitude of the surface AMR up to 9.3% at 24 T indicates that the surface state of CrSb₂ not only has the antiferromagnetic order but

also the strong spin-orbit interaction. Such exotic magnetic surface states could provide a new research arena for condensed matter physics and spintronics.

We thank Prof. Yusuke Kato and Prof. Saburo Takahashi for fruitful discussion. This work was performed at the High Field Laboratory for Superconducting Materials, Institute for Materials Research, Tohoku University (Project Nos. 202112-HMKPA-0015 and 202302-HMKPA-0061). Also, this work was carried out by the joint research of the Cryogenic Research Center, the University of Tokyo. This work was supported by JST FOREST Program, Grant Number JPMJFR203H and by JSPS KAKENHI, Grant Numbers JP21H01794, JP22H05449, JP22H04464, JP21K18890, JP22J21520, JP19H05600, JP19K03736, JP21H05470, JP22H04933, JP22H01176, JP23H01832, and JP22H00109. K.N. is supported by Research Fellowships of Japan Society for the Promotion of Science for Young Scientists.

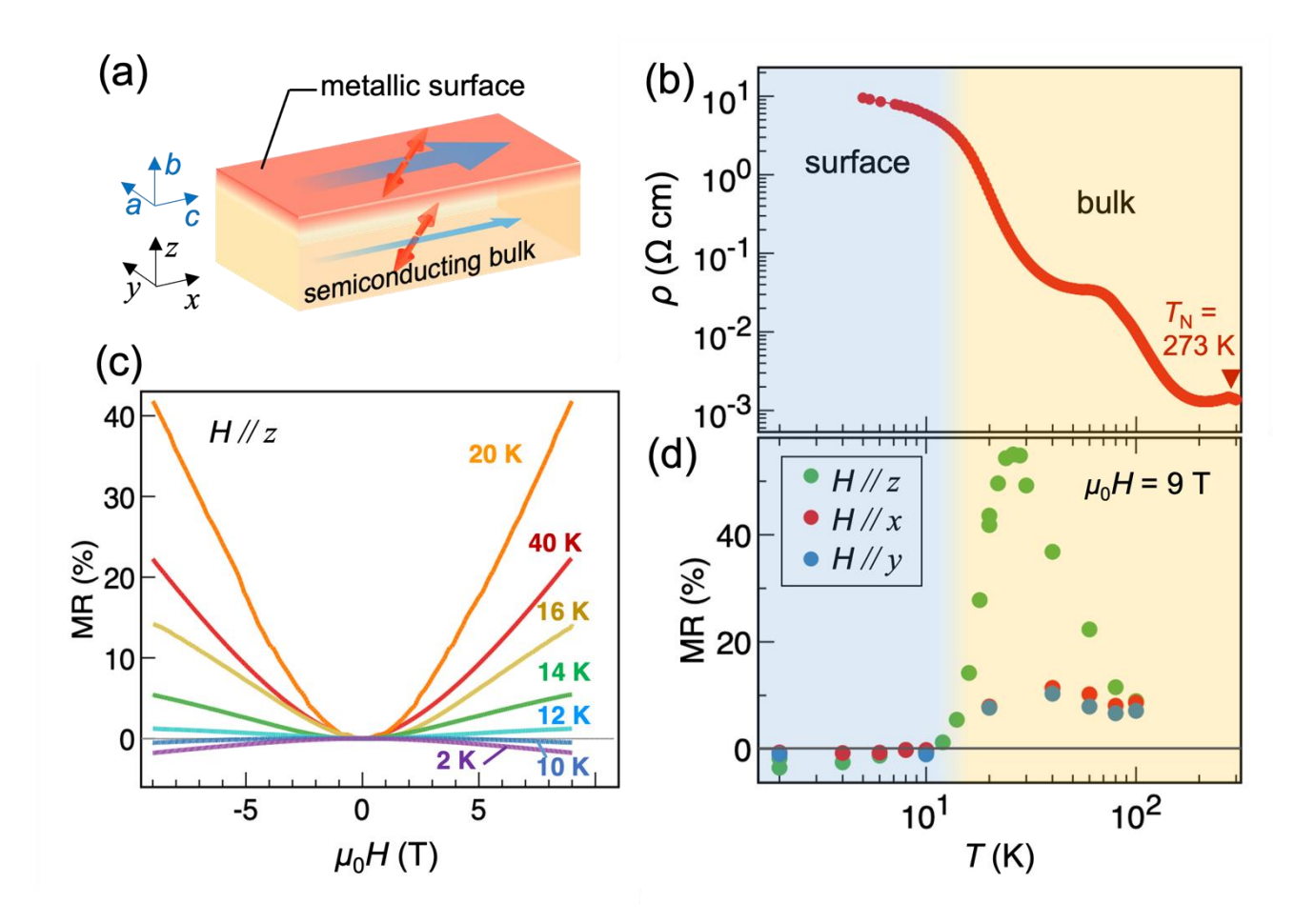


Fig. 1: (a) Schematic illustration of bulk and surface states of CrSb₂. The surface state is illustrated only on the top surface for simplicity. As to the relation between x, y, and z axes and the crystallographic axes, see text. The direction of electric current is represented by blue arrows, and that of antiferromagnetic moments by red arrows. The magnetic easy-axis lies in the xy plane and is tilted 61.5° from the x-axis. (b) Temperature dependence of electrical resistivity $\rho_{xx}(T)$ without magnetic field. The Néel temperature is shown by the red arrow. Temperature ranges dominated by surface and bulk conductions are colored blue and yellow, respectively. (c) Magnetic-field (H) dependence of magnetoresistance, MR (%) $\equiv 100 \times \{\rho_{xx}(H) - \rho_{xx}(0 \text{ T})\} / \rho_{xx}(0 \text{ T})$, at selected temperatures. The magnetic field is applied perpendicular to the sample plane, *i.e.* along the z-axis. (d) Temperature dependence of MR measured at 9 T applied along the x, y, and z axes. Temperature ranges dominated by surface and bulk conductions are colored as explained in (b).

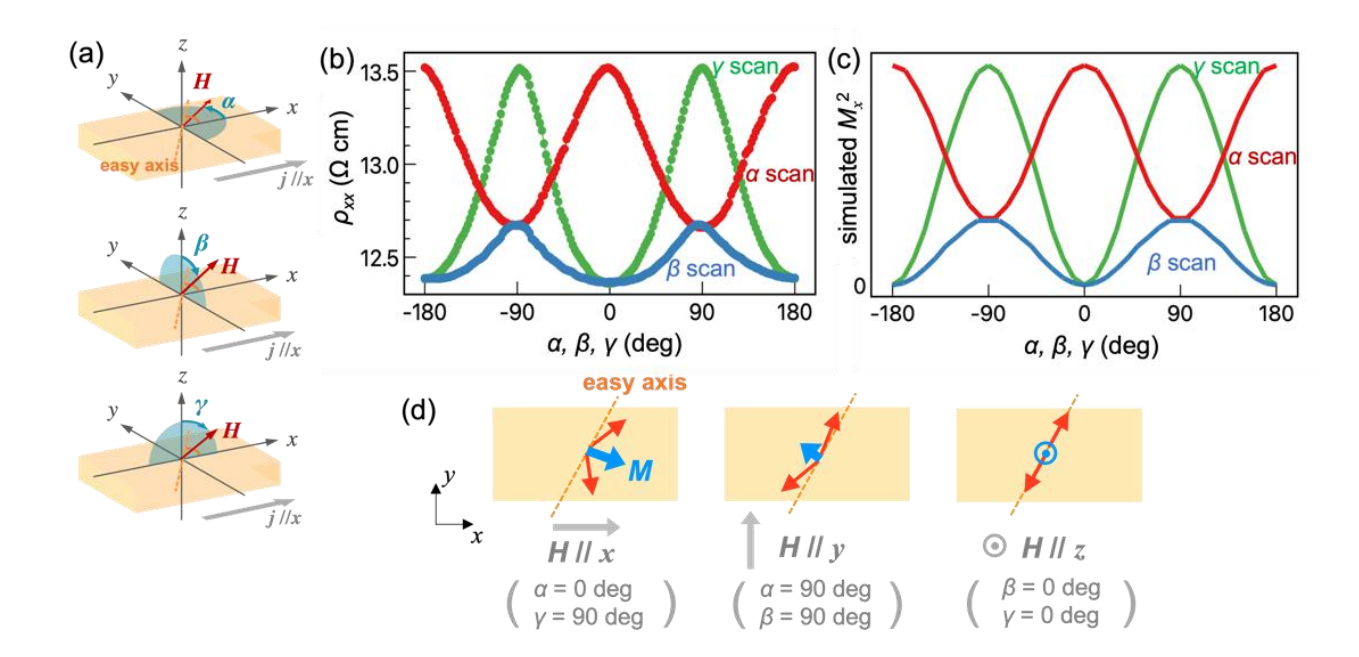


Fig. 2: (a) Sketches of the definition of angles α , β , γ and the measurement configuration of ADMR. (b) ADMR results of α , β , and γ scans measured at 24 T and 1.4 K. (c) Simulation curves of the angle dependence of the square of net magnetization along the x-axis (M_x^2) . (d) Schematics for the induced magnetic moments under the magnetic field applied along the x, y, and z directions. Red arrows indicate sublattice magnetization vectors and blue arrows indicate net magnetization vector within the xy plane. The schematics only show one magnetic domain for simplicity, while in the calculation, two magnetic domains with different easy-axis configurations are assumed to be equal and averaged. Tilt angles are exaggerated for easy viewing.

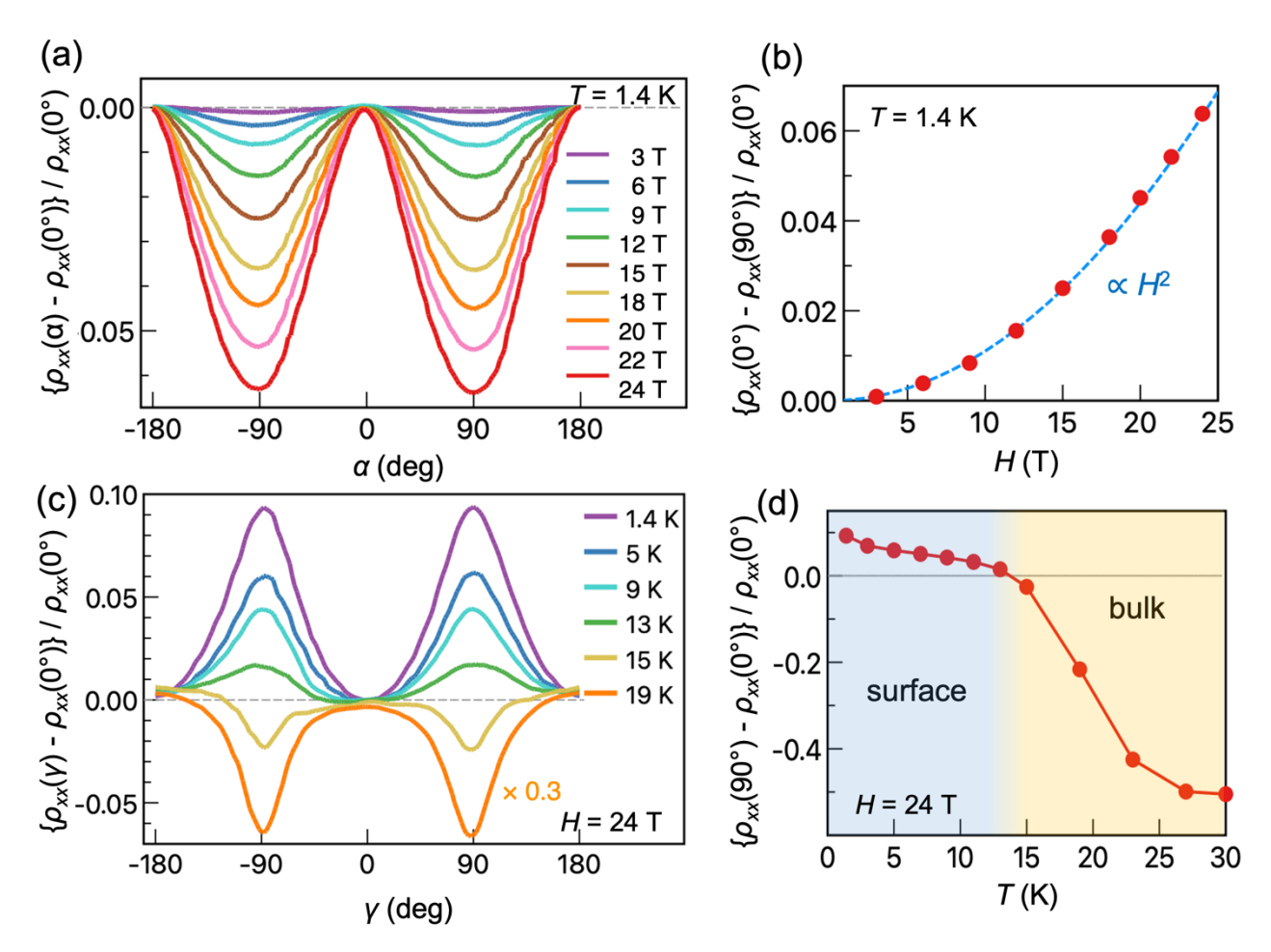


Fig. 3: (a) ADMR of α scan at 1.4 K measured under various magnetic fields up to 24 T. (b) Magnetic field (*H*) dependence of ADMR magnitude, $\{\rho_{xx}(\alpha=0^\circ) - \rho_{xx}(\alpha=90^\circ)\} / \rho_{xx}(\alpha=0^\circ)$, obtained from (a). The blue dotted curve is a quadratic function normalized to fit the experimental data. (c) ADMR of γ scan at 24 T measured at different temperatures ranging from 1.4 K to 19 K. (d) Temperature dependence of ADMR magnitude of γ scan at 24 T, $\{\rho_{xx}(\gamma=90^\circ) - \rho_{xx}(\gamma=0^\circ)\} / \rho_{xx}(\gamma=0^\circ)$, obtained from (c) and additional high temperature (>19 K) data. Temperature ranges dominated by surface and bulk conductions are colored blue and yellow, respectively, as in Figs. 1(b) and (d).

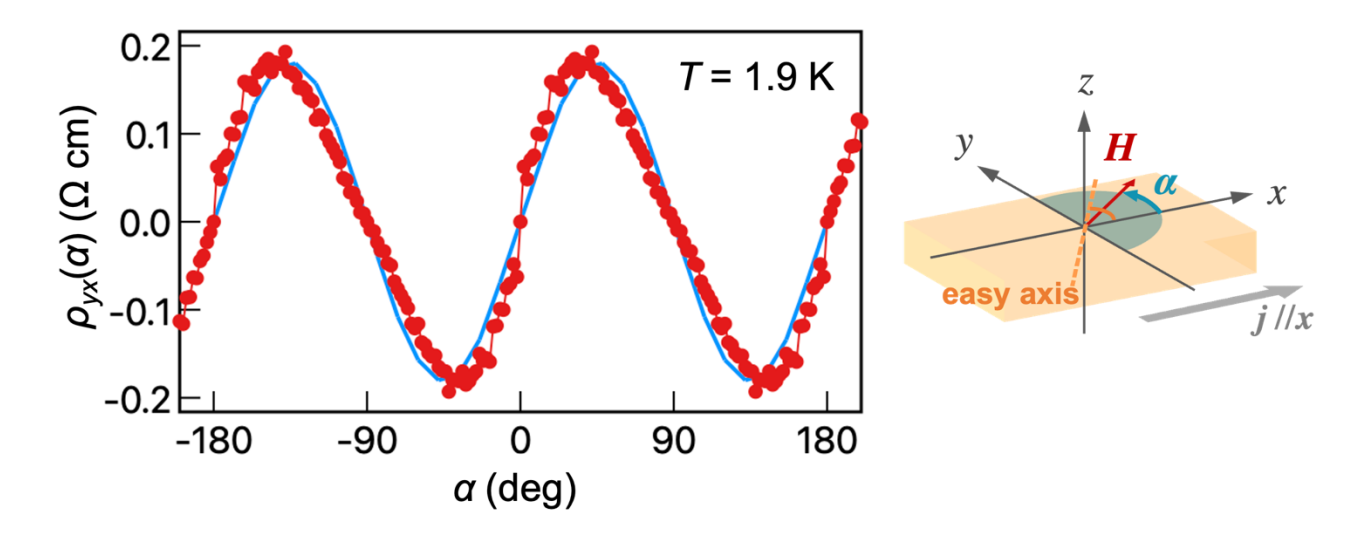


Fig. 4: ADMR data of α scan for transverse resistivity ρ_{yx} at 21 T and 1.9 K. The simulation curve of the angular dependence of the transverse AMR (planar Hall effect) signal is also shown by the blue curve. The sketch of the measurement condition is illustrated in the right panel.

- [1] J. M. Tomczak, *Thermoelectricity in correlated narrow-gap semiconductors*, J. Phys.: Condens. Matter **30**, 183001 (2018).
- [2] J.-H. Chu, Z.-Y. Mi, and D.-Y. Tang, Band-to-band optical absorption in narrow-gap Hg_{I-} ${}_{x}Cd_{x}Te$ semiconductors, J. Appl. Phys. **71**, 3955 (1992).
- [3] A. Winter, H. Pascher, M. Hofmayer, H. Krenn, T. Wojtowicz, X. Liu, and J. K. Furdyna, *Kerr Rotation and Magnetic Circular Dichroism Spectra of Ferromagnetic InMnSb and InMnAs*, Rev. Adv. Mater. Sci **20**, 92 (2009).
- [4] V. N. Antonov, B. N. Harmon, and A. N. Yaresko, *Electronic structure and magneto-optical Kerr effect of Tm monochalcogenides*, Phys. Rev. B **63**, 205112 (2001).
- [5] C. Petrovic, J. W. Kim, S. L. Budko, A. I. Goldman, P. C. Canfield, W. Choe, and G. J. Miller, *Anisotropy and large magnetoresistance in the narrow-gap semiconductor FeSb*₂, Phys. Rev. B **67**, 155205 (2003).
- [6] P. Rosa, Y. Xu, M. Rahn, J. Souza, S. Kushwaha, L. Veiga, A. Bombardi, S. Thomas, M. Janoschek, E. Bauer, *et al.*, *Colossal magnetoresistance in a nonsymmorphic antiferromagnetic insulator*, npj Quantum Materials **52**, 5 (2020).
- [7] R. Sultana, P. Neha, R. Goyal, S. Patnaik, and V. P. S. Awana, *Unusual non saturating Giant Magneto-resistance in single crystalline Bi₂Te₃ topological insulator, J. Magn. Magn. Mater. 428, 213 (2017).*
- [8] J. E. Moore, *The birth of topological insulators*, Nature **464**, 194 (2010).
- [9] M. Z. Hasan and C. L. Kane, *Colloquium: Topological insulators*, Rev. Mod. Phys. **82**, 3045 (2010).
- [10] M. Dzero, K. Sun, V. Galitski, and P. Coleman, *Topological kondo insulators*, Phys. Rev. Lett. **104**, 106408 (2010).
- [11] P. S. Riseborough, *Heavy fermion semiconductors*, Adv. Phys. **49**, 257 (2000).
- [12] S. Rachel, *Interacting topological insulators: a review*, Rep. Prog. Phys. **81**, 116501 (2018).
- [13] R. Hu, V. F. Mitrović, and C. Petrovic, *Anisotropy in the magnetic and electrical transport properties of Fe*_{1-x} Cr_xSb_2 , Phys. Rev. B **76**, 115105 (2007).
- [14] I. I. Mazin, K. Koepernik, M. D. Johannes, R. González-Hernández, and L. Šmejkal, *Prediction of unconventional magnetism in doped FeSb*₂, Proc. Natl. Acad. Sci. **118**, e2108924118 (2021).
- [15] G. Kuhn, S. Mankovsky, H. Ebert, M. Regus, and W. Bensch, *Electronic structure and magnetic properties of CrSb*₂ and FeSb₂ investigated via ab initio calculations, Phys. Rev. B **87**, 085113 (2013).
- [16] K.-J. Xu, S.-D. Chen, Y. He, J. He, S. Tang, C. Jia, E. Y. Ma, S.-K. Mo, D. Lu, M. Hashimoto, et al., Metallic surface states in a correlated d-electron topological Kondo insulator candidate FeSb₂, Proc. Natl. Acad. Sci. **117**, 15409 (2020).
- [17] J. B. Goodenough, *Energy bands in TX*₂ *compounds with pyrite, marcasite, and arsenopyrite structures*, J. Solid State Chem. **5**, 144 (1972).
- [18] H. Holseth, A. Kjekshus, and A. Andresen, *Compounds with the marcasite type crystal structure*,

- Acta. Chem. Scand. 22, 16 (1970).
- [19] Q. Du, H. Fu, J. Ma, A. Chikina, M. Radovic, B. Yan, and C. Petrovic, *Surface conductivity in antiferromagnetic semiconductor CrSb*₂, Phys. Rev. Res. **2**, 043085 (2020).
- [20] H. Takahashi, R. Okazaki, Y. Yasui, and I. Terasaki, *Low-temperature magnetotransport of the narrow-gap semiconductor FeSb*₂, Phys. Rev. B **84**, 205215 (2011).
- [21] B. C. Sales, A. F. May, M. A. McGuire, M. B. Stone, D. J. Singh, and D. Mandrus, *Transport, thermal, and magnetic properties of the narrow-gap semiconductor CrSb*₂, Phys. Rev. B **86**, 235136 (2012).
- [22] M. B. Stone, M. D. Lumsden, S. E. Nagler, D. J. Singh, J. He, B. C. Sales, and D. Mandrus, *Quasi-one-dimensional magnons in an intermetallic marcasite*, Phys. Rev. Lett. **108**, 167202 (2012).
- [23] A. B. Shick, S. Khmelevskyi, O. N. Mryasov, J. Wunderlich, and T. Jungwirth, *Spin-orbit coupling induced anisotropy effects in bimetallic antiferromagnets: A route towards antiferromagnetic spintronics*, Phys. Rev. B **81**, 212409 (2010).
- [24] T. R. McGuire and R. I. Potter, *Anisotropic magnetoresistance in ferromagnetic 3d alloys*, IEEE Trans. Magn. **11**, 1018 (1975).
- [25] H. Wang, C. Lu, J. Chen, Y. Liu, S. L. Yuan, S. W. Cheong, S. Dong, and J. M. Liu, *Giant anisotropic magnetoresistance and nonvolatile memory in canted antiferromagnet Sr₂IrO₄*, Nat. Commun. **10**, 2280 (2019).
- [26] H. Yang, Q. Liu, Z. Liao, L. Si, P. Jiang, X. Liu, Y. Guo, J. Yin, M. Wang, Z. Sheng, et al., Colossal angular magnetoresistance in the antiferromagnetic semiconductor EuTe₂, Phys. Rev. B 104, 214419 (2021).
- [27] J.-R. Soh, P. Manuel, N. M. B. Schröter, C. J. Yi, F. Orlandi, Y. G. Shi, D. Prabhakaran, and A. T. Boothroyd, *Magnetic and electronic structure of Dirac semimetal candidate EuMnSb*₂, Phys. Rev. B **100**, 174406 (2019).
- [28] T. Suzuki, L. Savary, J.-P. Liu, J. W. Lynn, L. Balents, J. G. Checkelsky, and H. Kong, *Singular angular magnetoresistance in a magnetic nodal semimetal*, Science **365**, 377 (2019).
- [29] T. G. S. M. Rijks, S. K. J. Lenczowski, R. Coehoorn, and W. J. M. de Jonge, *In-plane and out-of-plane anisotropic magnetoresistance in Ni₈₀Fe₂₀ thin films, Phys. Rev. B 56, 362 (1997).*
- [30] D. Kriegner, K. Výborný, K. Olejník, H. Reichlová, V. Novák, X. Marti, J. Gazquez, V. Saidl, P. Němec, V. V. Volobuev, et al., Multiple-stable anisotropic magnetoresistance memory in antiferromagnetic MnTe, Nat Commun 7, 11623 (2016).
- [31] C.-J. Zhao, L. Ding, J.-S. Huangfu, J.-Y. Zhang, and G.-H. Yu, *Research progress in anisotropic magnetoresistance*, Rare Met. **32**, 213 (2013).
- [32] See Supplemental Material at [URL] for the magnetization measurement; simulation results of the AMR and SMR; and the details information about the data analyzation of the transverse ADMR measurement. The Supplemental Material also contains Refs. [34,35].

- [33] H. Nakayama, M. Althammer, Y.-T. Chen, K. Uchida, Y. Kajiwara, D. Kikuchi, T. Ohtani, S. Geprägs, M. Opel, S. Takahashi, R. Gross, *et al.*, *Spin Hall magnetoresistance induced by a nonequilibrium proximity effect*, Phys. Rev. Lett. **110**, 206601 (2013).
- [34] M. Althammer, S. Meyer, H. Nakayama, M. Schreier, S. Altmannshofer, M. Weiler, H. Huebl, S. Geprägs, M. Opel, R. Gross, *et al.*, *Quantitative study of the spin Hall magnetoresistance in ferromagnetic insulator/normal metal hybrids*, Phys. Rev. B **87**, 224401 (2013).
- [35] Y.-T. Chen, S. Takahashi, H. Nakayama, M. Althammer, S. T. Goennenwein, E. Saitoh, and G. E. Bauer, *Theory of spin Hall magnetoresistance*, Phys. Rev. B **87**, 144411 (2013).